Astron. Astrophys. 320, 852–864 (1997)

ASTRONOMY AND ASTROPHYSICS

Line formation in Be star envelopes

II. Disk oscillations

W. Hummel[1,2] **and R.W. Hanuschik**[3]

[1] Astrofysisch Instituut, Vrije Universiteit Brussel, Pleinlaan 2, B-1050 Brussel, Belgium
[2] now at: Universitätssternwarte München, Scheinerstr. 1, D-81679 München, Germany
[3] Astronomisches Institut, Ruhr-Universität Bochum, D-44780 Bochum, Germany

Received 23 April 1996 / Accepted 13 September 1996

Abstract. We present numerical model calculations for an especially interesting class of Hα emission line profiles from Be star disks, those with asymmetric shape and long-term variability (so-called class 2 profiles). As an underlying model for the disk we investigate the hypothesis of Okazaki (1991) that these profiles are caused by a distortion of a quasi-Keplerian disk. The distortion has the form of a one-armed global disk oscillation (density and velocity wave).

The radiation transfer in the disk is calculated with an improved version of the spatially implicit 3D radiative transfer code of Hummel (1994).

The resulting sets of Hα emission line profiles reproduce well the observed structures of fully-resolved class 2 Hα emission lines, like double peaks and winebottle-type shoulders. For high inclinations, shell-type profiles result. It is shown that the full variety of observed profile shapes is caused by the interaction of kinematical and non-coherent scattering broadening. While this result has already been found by Hummel (1994) for the symmetric (class 1) Hα profiles, it is proven here for the second major profile class as well.

The comparison between observed and theoretical emission shows that the model of global disk oscillations is in full agreement with the observed shapes and the cyclic long-term variability of class 2 profiles.

Key words: line: profiles – line: formation – radiative transfer – stars: Be – circumstellar matter

1. Introduction

Emission lines from Be stars are produced in rotationally supported circumstellar disks, a picture still resembling very much the original ideas of Struve (1931). In the past decade, much progress has been made in understanding the kinematical and geometrical properties of these disks. High-resolution observations of optical emission lines have played a key rôle. In particular, Hα as a general indicator of the circumstellar disk state, and Fe II emission lines as tracers of the velocity field have turned out to be highly useful diagnostic tools.

The shape of most observed emission lines fall into two major classes (Hanuschik et al. 1988, 1996): Class 1 emission lines are symmetric, vary only slowly and supposedly arise in quasi-Keplerian disks in vertical hydrostatic equilibrium. The corresponding Fe II lines are double peaked. Class 2 emission lines have a characteristic asymmetry, and are usually variable in the long-term. In Fe II lines, the most extreme class 2 manifestation are the steeple-type profiles (see examples in Hanuschik et al. 1995). Within these classes, there exist subclasses which according to our interpretation depend on inclination (shell lines at high inclination, winebottle-type profiles at low inclination).

Class 1 Fe II lines in Be stars have successfully been modelled by Hanuschik (1988) using a rotating disk model. In a more general effort, Hummel (1994, henceforth Paper I) has solved the 3D radiative transfer problem for optically thick emission lines. While he studied symmetrical (class 1) profiles, we now extend his study to the second major class of Be emission lines; those of class 2.

Line profile asymmetry in optically thick lines requires radial motions and/or a non-axisymmetric density distribution. Since in class 2 Be stars both optically thick Hα emission and the optically thin Fe II emission lines are asymmetric, the major cause for line asymmetry has to be a non-axisymmetric velocity field in such disks. The simplest such configuration is an *elliptical* disk. This scenario was investigated, e.g., by Struve (1931), Johnson (1958) and Mc Laughlin (1961). The basic objection against large-scale elliptical disks is the expected rapid circularization due to gravitationally induced precession of orbits. Class 2 line profiles, however, have been observed to exist for decades (e.g. Dachs 1987).

A break-through was reached when Kato (1983) found that one-armed global disk oscillations (hereafter GDO) can exist in non-self gravitating, quasi-Keplerian disks. Okazaki (1991,

Send offprint requests to: W. Hummel, München address

henceforth O91) solved the equations of motions for a quasi-Keplerian disk with superimposed isothermal linear perturbations in density and velocity. The long-term variability in the disk is caused by a slow precession of the density wave due to the radial gas pressure. The wave pattern is predicted to rotate retrograde with typical periods of 2–12 years. This hydrodynamical model still contains many features of the elliptical disk, in particular the relation between peak strength and radial velocity shift.

In a further study, Papaloizou et al. (1992) neglected the influence of the gas pressure on the wave precession, but found instead a prograde wave pattern precession due to the flattening of the rapidly rotating central star.

Observational evidence for GDO is found from high-resolution spectroscopic studies. The long-term V/R (= ratio of violet to red peak fluxes, respectively.) variations of asymmetric Hα profiles and the shape of steeple-type class 2 Fe II emission lines are in agreement with the assumption of a large-scale GDO (Hanuschik et al. 1995).

The purpose of the present paper is to test Kato's and Okazaki's predictions in a more general way by modelling Hα emission line profiles of perturbed Be disks and comparing them to observed class-2 profiles.

2. Basic model assumptions

2.1. Central star and disk temperature

The model parameters used here are identical to those of O91. In detail our model consists of a central star of spectral type B5V ($\Longrightarrow M_\star = 6.46 M_\odot, R_\star = 3.8 R_\odot, T_{\rm eff} = 15\,000$K).

Since there are no observational contraints concerning the temperature distribution in Be star circumstellar disks, and since the theory of GDOs can only handle isothermal waves in the present state, we also adopt this assumption and use a constant temperature of $T_{\rm d} = 10\,000$K.

There are several indications for a rather flat or constant temperature distribution in Be star disks: *i*) unlike in accretion disks of dwarf novae, Ca II and He I emission lines do not occur at the same time, suggesting at least a much flatter temperature gradient for Be star disks than for CVs. *ii*) Isothermal models are able to explain many aspects of Be star spectra like line and continuum polarisation and optical flux (Poeckert & Marlborough 1978), IR-continuum excess (Waters 1987) and Hα emission lines (Paper I). However, a temperature gradient cannot be fully excluded. A radial decrease would emphasize the inner disk region for the emission lines.

Since there is no correlation between the product of mass loss rate and C^{3+} ionisation fraction and the Hα emission equivalent widths (Prinja, 1989) it is justified to neglect the influence of the stellar wind on the structure of the circumstellar disk.

2.2. Density distribution

For describing disk properties, we define the normalized cartesian coordinates $X \equiv x/R_*$, Y and Z (we normalize all coordinates to the stellar radius R_*) with their origin in the stellar centre and X, Y spanning the equatorial plane of the disk which coincides with the stellar equatorial plane. We furthermore use the polar coordinates $R = \sqrt{X^2 + Y^2}$ and φ which is counted counterclockwise from the positive X-axis.

We assume that vertical hydrostatic equilibrium is established between gas pressure gradient and Z-component of the stellar gravitation. This assumption is reasonable since i) many Be disks are observed to be quite stable over years, and ii) such hydrostatic equilibrium is the simplest physical configuration in the case of a rotating, axi-symmetrical structure. The density law in the radial direction is less well known. For simplicity we assume a power law dependence. The density distribution of the *unperturbed* disk is then given by

$$N_{\rm u}(R,Z) = N_0\ R^{-\alpha} \exp\left\{-\frac{Z^2}{2H^2(R)}\right\}\ . \tag{1}$$

The vertical scale height $H(R)$ is increasing with $R^{3/2}$,

$$H(R) = \frac{c_{\rm s}}{V_{\rm K}(R_*)} \cdot R^{3/2} \tag{2}$$

with $c_{\rm s}$ = isothermal sound speed and $V_{\rm K}(R_*)$ = Keplerian velocity at $R = 1$.

The density distribution of the *perturbed* disk, $N_{\rm p}$, is given by

$$N_{\rm p}(R,\varphi,Z) = N_{\rm u}(R,Z) \cdot \zeta(R,\varphi) \tag{3}$$

where

$$\zeta(R,\varphi) = 1 + a_{\rm G} n_{\rm G}(R) \cos\varphi \tag{4}$$

is the perturbation factor, describing the perturbed density $N_{\rm p}(R,\varphi,Z)$ in units of the unperturbed density $N_{\rm u}(R,Z)$. Only the fundamental mode of the perturbation is considered. The form of the perturbation function $n_{\rm G}(R)$ has been taken from O91 (his Figs. 5, 6) for the cases $\alpha = 2, 3$.

$a_{\rm G}$ is a free dimensionless amplitude factor. Since Okazaki's calculation is a linear treatment, his solution implicitely assumes small perturbations. As we will see, however, the observed line profile asymmetries are much too strong to be compatible with small perturbations. This is a situation requiring a nonlinear treatment which, however, is not at hand presently. We therefore refrain from reproducing all details of the observations, but rather intend to demonstrate that the basic properties of the asymmetric class 2 emission line profiles can be understood in terms of the GDO theory. Therefore we will formally permit in the following the range $a_{\rm G} = 0 \ldots 1$, but use the linear solution of O91, keeping in mind the physical limitations of this approach.

The disk starts at the stellar surface $R = 1$ and extends out to $R_{\rm d} = 5$. Fig. 1 shows contours of the density perturbation $n_{\rm G}(R)\cos\varphi$ in the equatorial plane of the disk. The density wave in the equatorial plane has a nodal ring at $R \approx 1.8$ and a nodal line at $X = 0$. The density distribution is symmetric with respect to the equatorial plane ($Z = 0$) and to the meridional plane defined by $Y = 0$. A maximum density region exists near

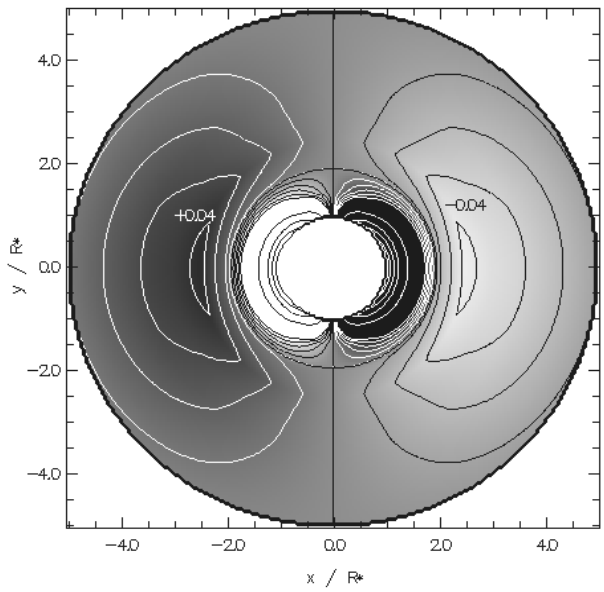

Fig. 1. Density perturbation function $n_{\rm G}(R)\cos\varphi$. White contours are positive density perturbations, while black contours indicate regions of density dilution compared to the unperturbed density law. The contours of the outer disk part beyond the nodal ring at $R \approx 1.8$ start from -0.04 (black contours) and go up to 0.04 (white contours) in steps of 0.01. The four contour lines near the stellar surface show values of 0.8, 0.6, 0.4 and 0.2 (black lines) and -0.2, -0.4, -0.6 and -0.8 (white lines)

$[X, Y] = [1.5, 0]$, and a corresponding density minimum at $[X, Y] = [-1.5, 0]$. For the limiting case $a_{\rm G} = 1$ and for $\alpha = 2$, the density $N_{\rm p}(R = 1, \varphi = 0, Z = 0)$ is twice as large as in the unperturbed case, and $N_{\rm p}(1, \pi, 0) = 0$. For $\alpha = 3$, the same holds at $R = -1$.

2.3. Velocity distribution

The velocity field of the unperturbed disk is assumed to be quasi-Keplerian: $V_\varphi = V_{\rm K}(R) \propto R^{-1/2}$, $V_R \approx V_Z \approx 0$, i.e. only small subsonic radial and vertical motions exist to establish vertical equilibrium and provide viscous transport of angular momentum. Following O91, the GDO-perturbed velocity field can be described by such Keplerian motion with a superimposed velocity perturbation. Let $\Delta V_\varphi(R, \varphi)$ and $\Delta V_R(R, \varphi)$ be the deviations from a purely Keplerian flow, in radial and angular directions, resp. Following O91 we assume that no distortion of vertical hydrostatic equilibrium occurs, i.e. $V_Z = 0$. The components of the velocity field then read:

$$\mathbf{V}(R, \varphi, Z) = \begin{pmatrix} V_R \\ V_\varphi \\ V_Z \end{pmatrix} = \begin{pmatrix} \Delta V_R(R) \sin\varphi \\ V_{\rm K}(R) + \Delta V_\varphi(R) \cos\varphi \\ 0 \end{pmatrix}, \qquad (5)$$

where $V_{\rm K}$ is the Keplerian velocity:

$$V_{\rm K} = \sqrt{\frac{GM_\star}{R_\star}} R^{-1/2} . \qquad (6)$$

The relation between the radial and angular components of the perturbation reads:

$$\Delta V_\varphi(R) = \frac{1}{2} \Delta V_R(R). \qquad (7)$$

The R-component of the perturbation velocity $\Delta V_\varphi(R)$ has to be multiplied with the free amplitude factor $a_{\rm G}$. It is also taken from Figs. 5 and 6 of O91 for cases $\alpha = 2, 3$.

The quantity relevant to the observer, located somewhere above or in the X, Y-plane, is the line-of-sight (radial) velocity $V_{\rm rad}$,

$$V_{\rm rad} = V(R, \varphi) \ \sin i \ \sin\varphi \ . \qquad (8)$$

Lines-of-sight towards an observer are characterized by the inclination i and azimuthal angle φ.

In Fig. 2a radial velocity contours in the equatorial plane (Doppler map) are shown for observer direction $\varphi = 0°$. The region between the stellar disk and the observer which appears projected onto the stellar disk for the observer located at $i = 90°$, the so-called shell volume, is indicated by two straight lines. In Figs. 2b, 2c and 2d similar Doppler maps for $\varphi = 45°$, $90°$ and $135°$ are shown.

These figures resemble the Doppler map of an unperturbed Keplerian disk in that the characteristic dipole pattern is preserved, but appears twisted. In particular, for aspects $\varphi \neq 0°$ or $180°$, the contour $V_{\rm rad} = 0$ is no longer a straight line, and the line-of-sight through the stellar centre divides the disk into halves which are asymmetric in radial velocity and density distribution.

Orbits in the distorted velocity field from Eq. (5) are ellipsoidal. If the observer is located at $\varphi = 0°$, Fig. 2a, the line-of-sight is the apsidal line. Eccentricity varies with radius.

3. Results of the standard model

Technical aspects of our computer code are treated in the Appendix. As the amount of computer time needed was extremely high (of the order of weeks), we have not been able to fully explore the parameter space. We have therefore started with a reference model which we will discuss in the following. The influence of some important parameters will be explored in the next section.

3.1. Line profiles

We have chosen the following set of parameters for our standard model (SM, or model 1): $N_0 = 10^{14}$ cm^{-3}, $a_{\rm G} = 1$, $R_{\rm d} = 5$, $\alpha = 2$, MK = B5V.

The resulting model emission lines are shown in Fig. 3. The line profiles are sorted in a matrix with columns showing sequences of increasing i, and rows of increasing φ.

3.1.1. Symmetric profiles, $\varphi = 0°$ and $180°$

Symmetric Hα emission lines, visible at $\varphi = 0°$ (first column) and $\varphi = 180°$ (last column), are similar in shape to emission

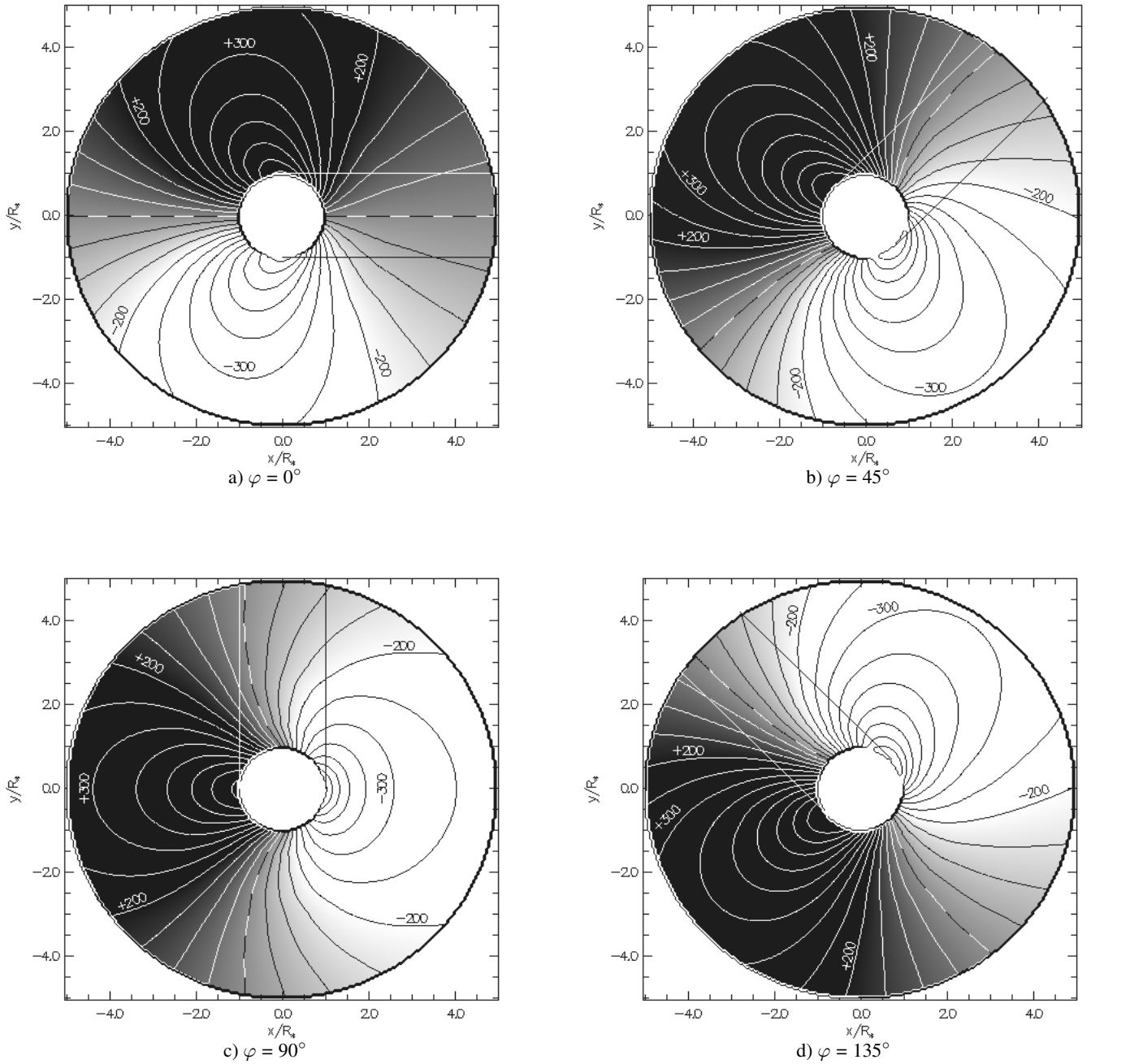

Fig. 2a–d. Radial velocity contours in the equatorial plane of the disk ($Z = 0$) as seen from an observer at **a** $\varphi = 0°$, **b** $\varphi = 45°$, **c** $\varphi = 90°$, and **d** $\varphi = 135°$. The increment between two contours is 50 km s^{-1}. Negative radial velocity regions (blueshifted) are indicated by black contours, while white contours show the regions of positive $V_{\rm rad}$. The dashed line shows the zero radial velocity contour. The two straight lines surround the shell region; they point to the observer. The particles in the disk are orbiting anti-clockwise

lines of unperturbed Keplerian disks (Hummel & Dachs 1992; Paper I). They are shaped by the following major broadening mechanisms:
(*i*) The *small-scale*, i.e. local, isotropic thermal broadening is described by a Gaussian distribution of thermal width $\Delta\lambda_{\rm th} = 0.28[T_{\rm d}/(10^4{\rm K})]^{1/2}$ Å.
(*ii*) The large-scale kinematical broadening due to differential rotation of the disk causes a double-peak profile usually visible in the inclination range of $20^\circ < i \leq 90^\circ$. This broadening mechanism is proportional to $\sin i$ and usually dominates the line broadening for $i > 20^\circ$, with $\Delta\lambda \simeq 10 - 15$Å.
(*iii*) The shear broadening (Rybicki & Hummer 1983; Horne & Marsh 1986) is an anisotropic scattering process due to the local velocity shear along the line-of-sight. This velocity shear, proportional to $\sin i \cdot \tan i$, causes a deep V-shaped depression yet still above the stellar continuum, visible around $i \approx 60^\circ$.
(*iv*) The non-coherent scattering broadening (NSB, Avrett & Hummer 1965) is an isotropic scattering process in optically thick media. For a finite slab its broadening profile has symmetric, sharp double peaks with a typical separation $\Delta\lambda_{\rm NSB} \simeq 3\Delta\lambda_{\rm th}$, and dominates the profile shape below $i \approx 15^\circ$. In Fig. 3, it causes peak merging at $i \approx 15^\circ$, and a complex 4-peak appearance at very small inclinations ($i \leq 5^\circ$). At larger inclinations it is responsible for the formation of flank inflections, the so-called winebottle-type profiles (Hummel & Dachs 1992).
(*v*) Finally, at high inclination ($i \gtrsim 70^\circ$) stellar radiation becomes absorbed by the disk in the *shell volume* (see Fig. 2a), and a deep central absorption additional to the emission component shows up.

Anisotropic, incoherent electron scattering, responsible for the extended smooth wings of many observed Hα profiles is not considered here since it is not important for the shape of the central part of the profiles.

3.1.2. Asymmetric emission lines

i) $i \leq 45^\circ$. Largest asymmetry occurs at $\varphi = 90^\circ$ and $\varphi = 270^\circ$, when the line-of-sight, projected on the disk plane, is perpendicular to the apsidal line.
ii) $i \gtrsim 45^\circ$. Peak splitting by non-coherent scattering becomes less and less important. Instead, shear broadening (assisted by shell absorption at even higher inclination values) takes over which shapes the central depression between the two peaks. At increasingly higher inclination the central depression becomes deeper and V-shaped. This is a consequence mainly of the length of the ray paths through the disk which increases with $\sec i$.
iii) $i = 90^\circ$. The most extreme case $F(90^\circ, 90^\circ)$ is again very useful for understanding the line shaping process. As Fig. 2 clearly shows, the largest fraction of material in the shell volume appears blueshifted to the observer, at radial velocities 0 ... -200 km s^{-1}. The corresponding contours run almost parallel to the line of sight, resulting in large column depth of absorbing matter and low photon escape probability. Consequently a blueshifted deep shell absorption trough emerges at large inclination from the blueshifted V-shaped central depression. Its wing on the blue side is deep enough to depress the flux of the blue peak of the net profile (shell absorption plus emission from the disk volume outside the shell volume) as well.

On the other side, the largest velocity shear (associated with the largest photon escape probability) occurs at angles $\pm 45^\circ$ between the radial velocity contour and a crossing line-of-sight (Horne & Marsh 1986). This is the case here for contours $V_{\rm rad} \gtrsim +100\,{\rm km\,s^{-1}}$, with the consequence that emission there is considerably stronger than at the corresponding blue part of the profile. Both effects (blue shell absorption and red increased escape probability) act together to reverse the observed V/R ratio from its values > 1 at low inclination to < 1 at high inclination.

3.2. Azimuthal profile sequences: observable quantities

The perturbation pattern (fundamental mode) of the disk is predicted to rotate with a period of 2–12 years depending on disk radius and density slope (O91). An azimuthal profile sequence with increasing φ corresponds to a retrograde rotation of the density-velocity wave. Therefore rows in Fig. 3 show a *chronological evolution* of line profiles and can be compared to the observed long-term variability of Be star emission lines. The reproduction of this typical variability pattern of profile shapes is, besides a comparison of model and observed line profiles, the most important application of our model calculations.

Such long-term variations of observable emission line parameters are collected in Fig. 4 for the standard model. The upper left plot shows the evolution of equivalent width W_α with azimuth φ.

The flux of the central depression, $I_{\rm cd}(\varphi)$ (upper right panel of Fig. 4) shows a large drop between $i = 70^\circ$ and $i = 80^\circ$, a consequence of shell absorption setting in at 80° due to the effective opening angle of the disk of about 14° (Paper I). It is interesting to note that $I_{\rm cd}$ is not symmetric around $\varphi = 90^\circ$.

The ratio $V/R = (I_{\rm v} - 1)/(I_{\rm r} - 1)$ of the peak intensities is shown in the lower plot for $i = 45^\circ, 60^\circ, 75^\circ$ and 90°. The V/R amplitude is increasing with inclination. Moreover, V/R changes sign near $i = 60^\circ$ which is due to the increasing influence of the shell trough over the emission peaks.

4. Parameter variations

The line formation mechanisms discussed in the foregoing section are sensitive to physical parameters like density and temperature. The next logical step is to explore the parameter space and calculate emission lines of model disks with physical parameters different from those in our standard model. Important parameters are the oscillation amplitude $a_{\rm G}$ and the radial slope of the density law α.

4.1. Amplitude $a_{\rm G}$ of the density wave: model 2

O91 has calculated density and velocity perturbations in a linear approximation. Perturbations of some 10% amplitude can be treated as linear. However, they produce line profiles which are only slightly asymmetric, much less than many observed class 2 profiles. Clearly, real GDO's in Be disks may become much

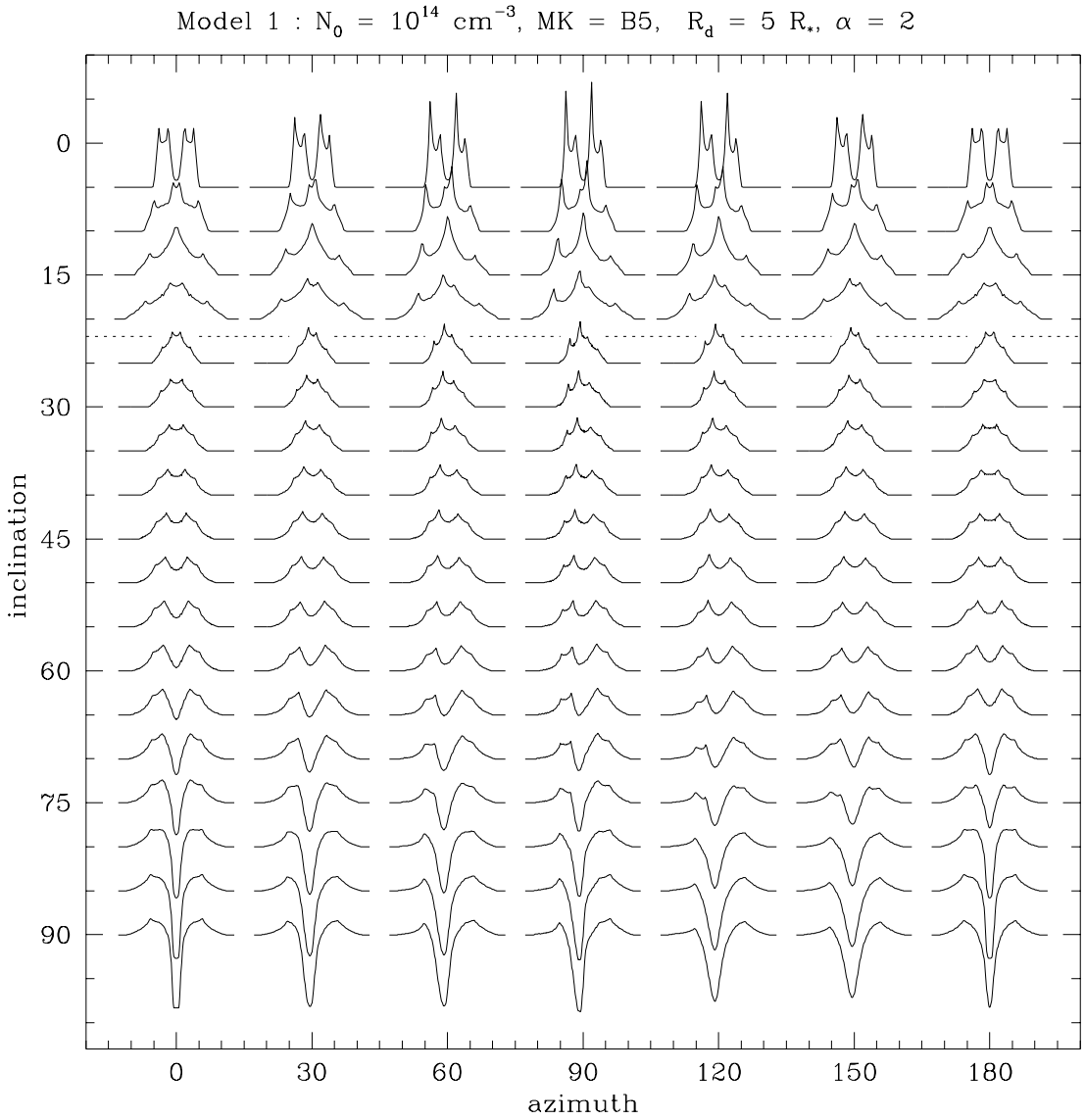

Fig. 3. Model Hα emission lines resulting from our standard model SM. Rows show sequences for increasing azimuthal angle φ, while columns show sequences for increasing i. As a consequence of the symmetry of the radial velocity field about the apsidal line (Fig. 2), model profiles for $180^\circ < \varphi < 360^\circ$ are obtained if the corresponding profile for $\varphi' = 360^\circ - \varphi$ is taken and mirrored. The flux unit is the stellar continuum F_c, corresponding to two tickmarks on the ordinate ($\widehat{=}\ 10^\circ$). 10° on the abscissa correspond to a wavelength interval of 5 Å for the four uppermost rows ($i \leq 20^\circ$), and 12.5 Å for the others ($i > 20^\circ$)

stronger and require a non-linear treatment. Such is not available at present. Therefore oscillation amplitudes of $a_G > 0.1$, as used here, are very crude extrapolations and meaningful only in obtaining a qualitative description of the main line shaping processes.

As long as the inclination is not too large, profiles from this model are very similar to those of model SM with $\varphi = 0^\circ, 180^\circ$ (Fig. 3, leftmost and rightmost columns). For edge-on view ($i > 70^\circ$), the intensity of the central depression I_{cd}/F_c in model 2 is intermediate between the two extreme cases in model SM. This follows from the amount of matter in front of the star which in model 2 is higher than in model 1, $\varphi = 180^\circ$, and lower than in model 1, $\varphi = 0^\circ$, respectively.

4.2. Radial density slope α: model 3

O91 has calculated wave patterns for various slopes of the unperturbed density, α. From his solutions, we have selected $\alpha = 3$ for the parameter study (model 3). Compared to the $\alpha = 2$ disk, the wave pattern for $\alpha = 3$ is phase-shifted by π. Because the total amount of disk material is much smaller in model 3 than in an $\alpha = 2$ disk, we have chosen a footpoint density $N_0 = 10^{15}$ cm^{-3} to obtain line profiles of comparable equivalent width.

Line profiles of model 3 are shown in Fig. 5. Due to the steeper density gradient, the inner regions with the highest wave amplitude are enhanced compared to $\alpha = 2$ models. These inner disk regions are those with strongest $\partial S/\partial z$, and therefore

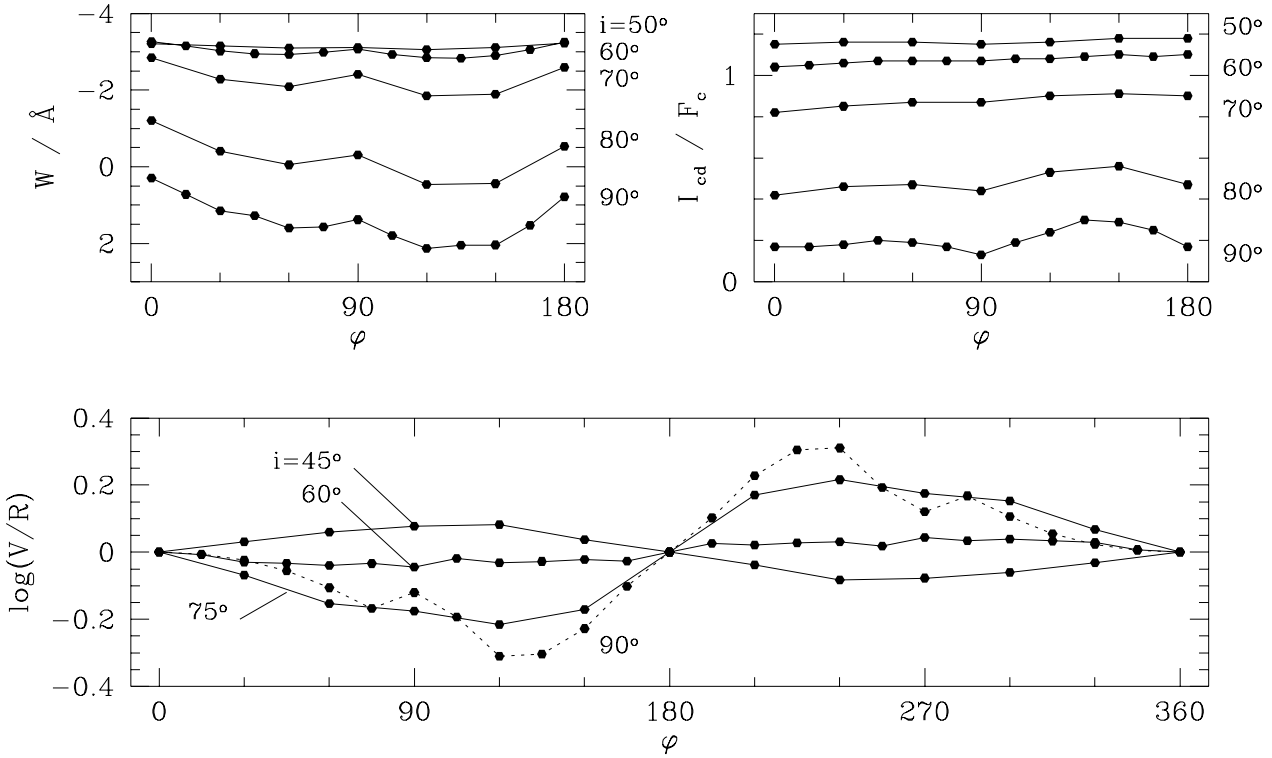

Fig. 4. Azimuthal sequences of four observable emission line parameters for the standard model at different inclinations i. Upper left: Hα equivalent width $W/$Å upper right: intensity of the central depression, $I_{\rm cd}(\varphi)/F_c$, lower plot: log(V/R), (dotted line: 90°)

model 3 produces slightly larger peak splitting due to NSB (see Paper I). The V/R-ratio as function of φ is shown in Fig. 6. The line profiles are very similar with respect to the SM, because the perturbation functions $n_{\rm G}$ and $\Delta V_{\rm R}$ are very similar for α = 2 and α = 3.

5. Comparison with observations

5.1. The data

The main motivation for our model calculations is to demonstrate that the shapes of class 2 Hα profiles from Be stars and their time variability pattern are compatible with the assumption of a disk hosting a precessing density wave. We will now compare our model profiles to observed Hα profiles.

These observations have been taken from the Bochum atlas of high-resolution emission and shell lines in Be stars (Hanuschik et al. 1996). These data provide for many Be and shell stars a decade-long survey of Hα and Fe II emission and shell lines. Some of these data have been published earlier by Hanuschik (1986) and Dachs et al. (1992).

5.2. Fitting procedure

Our two-level model atom approach without continuum is probably over-simplified and generates systematic errors in the calculated line intensities. Since the primary goal, however, is to investigate the profile shape, we simply follow Paper I and scale the model profiles $F_{\rm mod}$ by a free factor ξ to obtain the fits $F_{\rm fit}$,

$$F_{\rm fit} = F_{\rm c} + \xi\,(F_{\rm mod} - F_{\rm c})\ . \qquad (9)$$

This procedure is not applicable, however, for shell profiles with significant absorption components. Since a decomposition of observed line profiles into shell and emission component is not possible without invoking further assumptions, we have not treated shell profiles here.

We have furthermore smoothed the model profiles to remove numerical noise. Gaussians with smoothing width s have been used. This smoothing has negligible impact on the peak intensities. Fully resolved observed profiles often are even smoother because of the influence of electron scattering (which is omitted in the calculations).

Observed profiles have been corrected for the corresponding stellar peculiar velocity, $V_{\rm pec}$. Usually this parameter has been taken from the Bright Star Catalogue, but in some cases with obvious deviations it has been treated as a free parameter.

We have demonstrated in the previous section that within the parameter space investigated here, the main parameters influencing the profile shape are (i) azimuth φ and (ii) inclination i. The disk radius $R_{\rm d}$ is also likely to be important via the peak separation as in optically thin profiles and via the equivalent width W_α. However, we have not calculated a model with $R_{\rm d} > 5$ since no such solution is available from O91 for the disk perturbation.

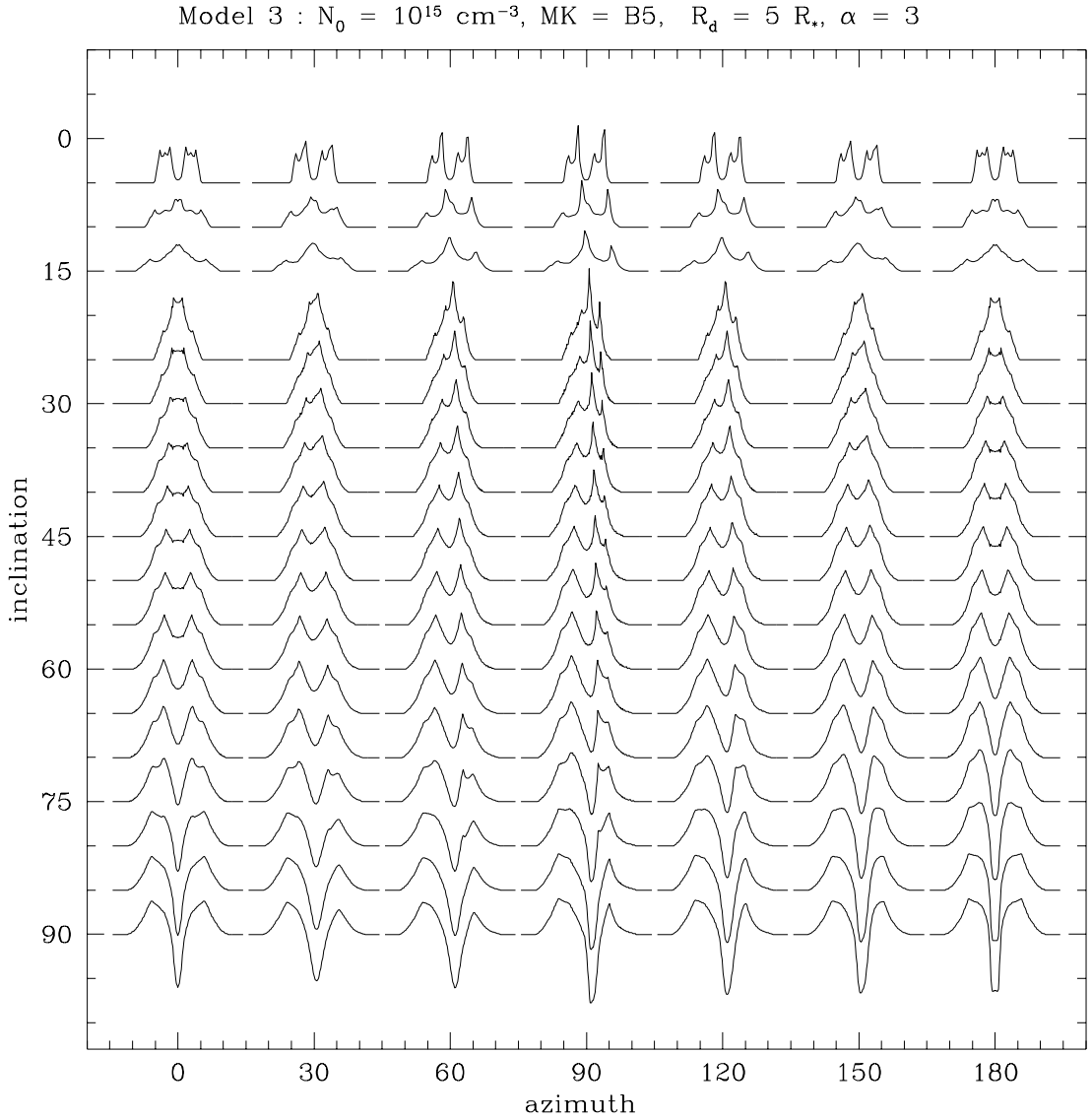

Fig. 5. As Fig. 3, for a density slope α = 3 and N_0 = 10^{15} cm^{-3}. Model profiles are flux-scaled such that for $i \leq 15°$, one tickmark corresponds to 1.67 F_c, and for $i > 15°$, 0.5F_c. The abscissa scales are the same as in Fig. 3

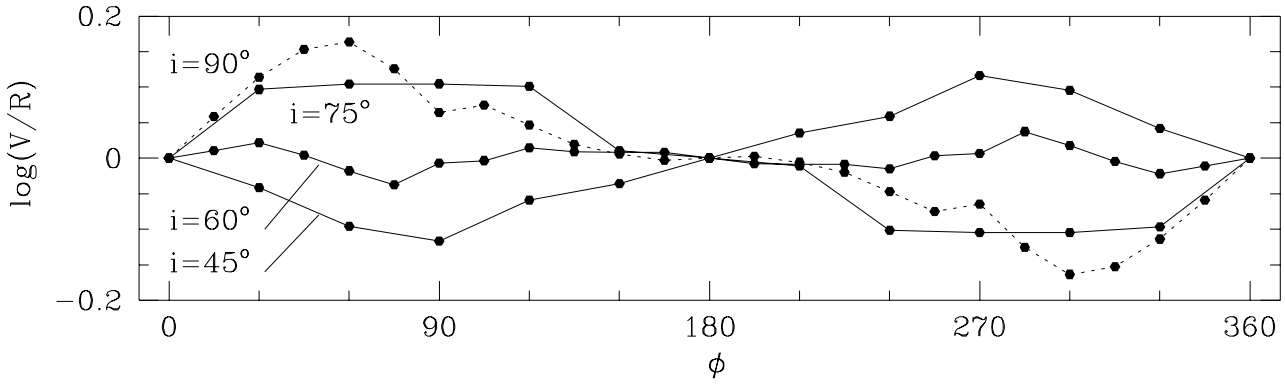

Fig. 6. V/R-ratio as a function of azimuth for model 3

Table 2. Parameters of the profile fits. Note that all models have been fitted with fixed parameters MK = B5V,α = 2, and $R_{\rm d}$ = 5.

Observational parameters					Fit parameters			
Star	MK[a]	$v \sin i$[a]/ km s^{-1}	$V_{\rm pec}^{b}$/ km s^{-1}	date[c]	log(N_0/cm^{-3})	i °	φ °	$V_{\rm pec}$/ km s^{-1}
HR 3858	B5Ve	260	26	870209	14	30	345	10
				930418	14	30	15	10
δ Cen = HR 4621	B2IVe	220	11	850102	14	20	90	11
				870208	14	20	180	11
				890304	14	20	270	11
				920111	14	20	330	11
α Ara = HR 6510	B3Ve	250	0	850228	14	30	0	0
				920324	14	30	0	0
66 Oph = HR 6712	B2IV–Ve	240	-13	891001	14	25	90	-11
				920324	14	25	330	-11

[a] Slettebak 1982
[b] Bright Star Catalogue
[c] Sources: 1985 – Hanuschik 1986; 1987 – Dachs et al. 1992; all other: Hanuschik et al. 1996

Table 1. Fit parameters

Parameter	meaning	range
$V_{\rm pec}$ [km s^{-1}]	stellar peculiar velocity	BSC* or free
MK	MK type	B5V (fixed)
i	inclination	free
log(N_0/cm^{-3})	footpoint density, Eq. (1)	13–15 (free)
α	density slope, Eq. (1)	2 (fixed)
$R_{\rm d}$	outer disk radius	5 (fixed)
s [km s^{-1}]	smoothing paramater	15...30 km s^{-1} (free)
φ	azimuthal angle (Eq. 8)	free
ξ	intensity scaling (Eq. 9)	free
$a_{\rm G}$	perturbation amplitude (Eq. 4)	1 or 0

* Bright Star Catalogue

We have fixed in the profile fits the disk temperature via the MK type (B5V), the density slope (α = 2), and the disk radius (5). Table 2 shows an overview of the fit parameters.

5.3. Comparison

We have fitted three groups of profiles: (i) unperturbed disks (class 1), (ii) perturbed disks (class 2) with large amplitude $a_{\rm G} \approx 1$, (iii) class 2 profiles with moderate amplitude $a_{\rm G} \ll 1$.

5.3.1. Class 1 profiles

HR 6510 = α Ara. We include this class 1 star with an unperturbed disk for demonstrating those principle properties of our model profiles which are not affected by the perturbation. Fits to two observed Hα profiles are shown in Fig. 7. For facilitating the interpretation we have also sketched in the upper left part the two major shaping effects: kinematical broadening causing kinematical peaks k_v, k_r (which are visible in optically thin lines, e.g. Fe II), and broadening by non-coherent scattering yielding shifted peaks p_v, p_r and shoulders s_v, s_r in Hα and other optically thick lines.

Our model is capable of reproducing (i) the two-peak structure of the measured profiles (p_v, p_r), (ii) the relative depth and shape of the central depression, (iii) the overall width, except for the extended wings in the data which are not reproduced in our model due to the neglect of Thomson scattering. The winebottle structure (s_v, s_r) is much fainter in the data than in the models. Thus the winebottle inflections found in the data are reproduced by the model, but are too strong and appear at too low an intensity. As we will see, this is a general drawback of our models. There are several reasons for this:

The application of a two-level model atom to Hα is approximately valid, but the incorporation of a more complex model atom including a correct handling of the ionisation equilibrium would significantly improve the physics of the model. Another origin is certainly the coarse spatial resolution of the disk close to the star, which implies large steps of $\Delta\tau_{\rm z} = \kappa\Delta Z$. This region of largest gradient in $\partial S/\partial z$ is resolved with only four or five gridpoints in the Z-direction and the pure NSB profile at $R \simeq 1$ is only approximately represented.

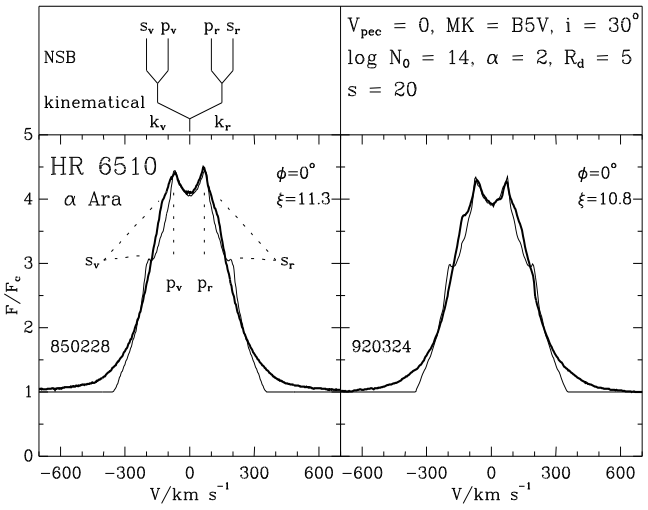

Fig. 7. Comparison of observed (thick lines) and calculated (thin lines) Hα emission lines, for HR 6510 = α Ara. The dates of measurements are given as 850228 = 1985, Feb. 28. The source for all observed profiles is Hanuschik et al., 1996. All model profiles are scaled by an arbitrary factor ξ. See text and Table 2 for meaning of the parameters. The influence of NSB broadening on kinematically broadened profiles is sketched in the upper left part; the position of the shoulders s and peaks p in the 1985 profile and in the model is sketched as well

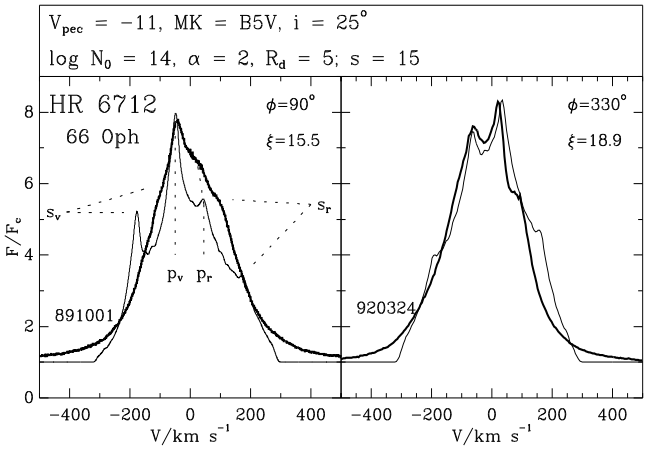

Fig. 8. Same as Fig. 7, for HR 6712 = 66 Oph

Another source of overestimated NSB is also the rather small circumstellar radius of R_d = 5, while disk radii derived from Hα peak separations (and corrected for peak splitting due to NSB) reveal in the mean larger emitting disk radii of $R_d \simeq 14$ (Hummel & Vrancken 1995). The inner regions of a larger radius disk ($R_d > 5$) would contribute pro rata less to the emission line profile with respect to the current small radius disk. The two peaks of the NSB profile at $R_d \simeq 14$ would be less separated because of a lower gradient $\partial S/\partial z$ and consequently the shoulders of the whole emission line profile would be less pronounced.

It should also be noted, that emission lines of large radii disks would be stronger and (keeping v_0 fixed) also narrower via a smaller FWHM. In this case, the scaling factor ξ would be closer to 1, meaning a better agreement between intensities of observed and calculated profiles.

5.3.2. Class 2 profiles, large amplitude

The next two stars (HR 6712, 4621) have shown at times steeple-type Fe II profiles in our profile record which are interpreted as being due to *strongly* distorted disks. They are the best candidates for a successful fitting with our a_G = 1 models.

HR 6712 = 66 Oph. This Be star has been investigated by Hanuschik et al. (1995) in some detail. It presently exhibits prototype class 2 behaviour. In 1989, the best fit is obtained (Fig. 8) for φ = 90°, in 1992 for φ = 330°. Our model for 1989 is capable of fitting the strong, dominating peak p_v, the correct $V > R$ behaviour (though not precisely the observed value), approximately the correct position of p_r and the presence of the red, almost suppressed inflection s_r. It grossly overestimates the blue shoulder s_r, predicting a strong subordinate peak instead of a smooth shoulder. This is again a consequence of the overestimate of NSB in the source function. In 1992, most profile properties, especially the V/R ratio and the depth and shape of the central depression, are well reproduced. Again, the winebottle structure is overestimated in strength, but the relative ratio is fitted properly.

The rather low value of i partially results from the influence of the strong NSB in the models: stronger NSB broadens the profiles over their kinematical value, and our "naive" fitting procedure compensates for that by a lower inclination value.

HR 4621 = δ Cen. We have fitted a sequence of four Hα obervations of this star between 1985 and 1992 (Fig. 9). These fits show that the density wave has almost completed a full cycle over that period. Both the data and the models show great similarity with the 66 Oph profiles (see above). Again, the NSB overestimates the winebottle structures, but their relative strength and that of the peaks are fairly well reproduced.

5.3.3. Class 2 profiles, low amplitude

HR 3858. This star is selected here since it only shows faint V/R variability in the Bochum atlas throughout 1985–1993 and very faint asymmetry in the Fe II lines. It probably represents a case of *lower amplitude* in the density wave. We may expect that corresponding models (which we have not calculated explicitely) are very similar to those for $a_G \approx 1$ if φ is close to 0°. We have fitted two such models and find the results quite successful, especially the fit for 1987 (apart from the notorious overestimate of winebottle structure).

6. Conclusions

The results of Paper I and this paper clearly demonstrate that the main profile shapes of optically thick Hα lines from Be star disks, though apparently rich in differences (see Hanuschik et al. 1996), are simply caused by the combined interaction of kine-

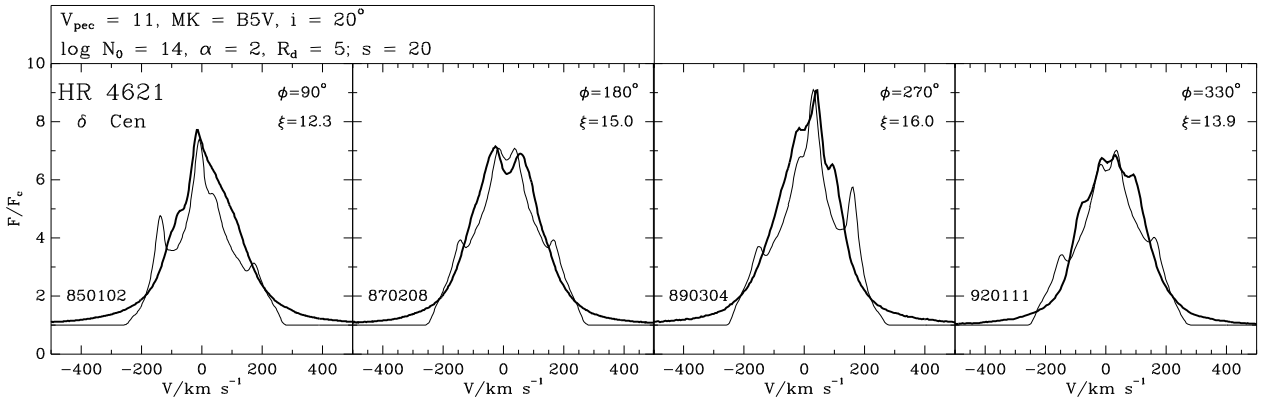

Fig. 9. Same as Fig. 7, for HR 4621 = δ Cen

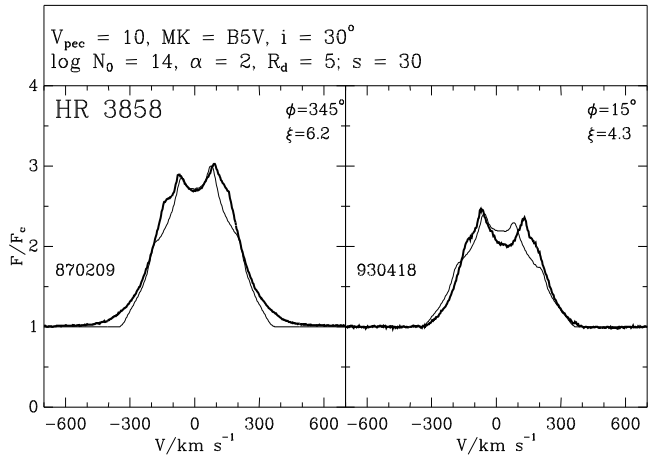

Fig. 10. Same as Fig. 7, for HR 3858

matical broadening and broadening by non-coherent scattering. We have shown in this paper that this very important result is valid for so-called class 2 profiles as well, i.e. for those with asymmetric and cyclically variable shape.

We have furthermore shown that the assumption of a density distortion causing the line profile asymmetry is compatible with the observed line profiles. Though a realistic description of the density distortion is still missing, we have found, by using a crude extrapolation of Okazaki's (1991) linear solution to large amplitudes, that the most obvious line profile properties can be reproduced by such a model. A drawback of our model is its systematically too high value for the NSB broadening function which is mostly due to the finite spatial resolution close to the star and due to rather small model disk radius.

The excessively large computing times needed for the calulation of our models have prevented an improvement of this drawback, as well as a more thorough investigation of the full parameter range. The following conclusions, however, already give some insight:

– There is not much information in the optically thick Hα profiles about the exact density structure, i.e. about N_0 and α (apart from the fact that for reasonable emission strength, $N_0 \geq 10^{14}$ cm^{-3} is required). This is not surprising, since despite the increased transparency of the disk due to velocity gradients, we mainly see surfaces of constant radial velocity, rather than the whole disk volume. In this situation, information about the exact shape of the density perturbation will be limited as well.
– The inclination is generally underestimated in our fits. The overestimated $\Delta V_{\rm NSB}$ causes an artificial broadening of the model profiles which will be reflected in inclination values systematically too low.
– The major positive result about our model fitting clearly is that both the shapes of asymmetric Hα profiles, and their cyclical time variability pattern, can be reproduced by a model disk which has the density structure of a hydrostatic disk perturbed by a density wave, as devised by O91. This is the last and most important cornerstone for supporting the hypothesis that the well-known long-term V/R variations of Be star emission lines result from a distorted disk.

The actual form of the perturbation pattern remains undetermined. The fact that the calculated emission lines with $a_{\rm G}$ = 1 are quite similar to observed ones give rise to the hope that the solution of a nonlinear perturbation theory is probably not too different from that of a linear perturbation. A more detailed insight may be gained from the investigation of optically thin emission lines.

The transitions from one profile shape to another (in case of V/R variability) are known to occur slowly and smoothly (see Hanuschik et al. 1995 for more detailed profile records). We find cycle times of the order of about 10 years from our stars with profile fits, except for HR 3858 where the duration time might be 5–6 times longer.

Acknowledgements. We would like to thank Dr. T. Okazaki for highly valuable discussions about his calculations. Grants by the *Deutsche Forschungsgemeinschaft* (Da 75/12–2) and by the *Service Centres and Research Networks* initiated and financed by the Belgian Federal Scientific Services (No. SC/005) are gratefully acknowledged. We also thank the *Wissenschaftlichen Ausschuß für die Landesgroßrechner Nordrhein-Westfalen* (WAL) for providing computing

time on a SNI S600/20 at the RWTH Aachen. The comments of the anonymous referee helped improve the discussion of the paper and are gratefully acknowledged.

Appendix

A.1. Numerical aspects

The problem of computing emission line profiles for a circumstellar disk undergoing GDO is solved using the spatially implicit 3D radiative line transfer code for a two-level atom with complete redistribution in the observer's frame. The method is treated in detail in Paper I.

As argued in Paper I, we assume Lyα to be optically thick and in detailled balance but are aware of the fact that coupling of Balmer lines to the continuum will influence the n=3 level population. Intensities of calculated emission lines are therefore unterestimated.

In the following we will list some general properties of our calculations. We use $N_X = N_Y = 81$, $N_Z = 40$ spatial gridpoints, scanning an area of $0...10R_* = 2R_\mathrm{d}$ in the X, Y-plane. The Z-direction is scanned between $Z = -1$ and +1 (one scale height at the outer rim of the disk is $H(5) = 0.25$). The stellar disk is resolved with the same grid.

Because of the symmetries of the problem, only one quarter of the solid angle 4π is scanned nearly homogeneously by 21 directions, giving 84 directions for the full solid angle 4π. The spectral flux is scanned by 160 wavelength gridpoints in the interval of $-16\text{Å} < \lambda < 16\text{Å}$, giving a spectral resolution of $\Delta\lambda = 0.2\text{Å}$ (or $\Delta V = 9\ \mathrm{km\,s^{-1}}$ at Hα). Note that the thermal width of hydrogen is $\Delta\lambda_\mathrm{th} = 0.28\text{Å}$ ($\widehat{=} 12.8\ \mathrm{km\,s^{-1}}$) at $T = 10\,000$K. Usually 13 iterations were necessary to achive an accuracy of the source function S of $\Delta S/S < 10^{-3}$.

After the convergence of the Λ^*-iteration for the source function, a set of 157 emission lines covering the aspect range of $0° < i < 90°$, $0° < \varphi < 180°$ is calculated for each model. $N_\lambda = 200$ wavelength gridpoints are used to calculate the final emission line profile.

All computations have been performed by one of us (WH) on a TRACE 7/200 and workstations at the AI RUB, a Cyber 922 at the RUB computing centre, CD/4000s and a CRAY-YMP at the ULB/VUB computing centre and a workstation at the KSB/ORB. The amount of computer time was extremely high (e.g., 2 weeks for the SM on a SUN SPARC 10 workstation, 5 days were needed for the iteration of the source function while the calculation of the 157 emission lines needed again about 9 days).

A.2. Improvement of code

The 3D radiative line transfer code has been improved and corrected with respect to Paper I.

A factor $(\sqrt{\pi}\Delta\lambda_\mathrm{th})^{-1}$ which normalizes the local broadening function to unity was omitted in Eq. (3) of Paper I. It has been inserted here. As long as the line absorption coefficient κ_l is treated as a free parameter, this factor is merely a scaling factor [Adam 1990, Eq. (5); Hummel & Dachs 1991]. In Paper I, were κ_l is calculated from an occupation density, this scaling factor results in an incorrect relation between N_0 and $\bar{J}$. A new calculation of the profiles from Paper I with the properly normalized ($\int_{-\infty}^{\infty}\phi_\lambda d\lambda = 1$) profile function yields emission line profiles with lower intensity but without changes in the profile shapes. Footpoint densities N_0 of Paper I have to be multiplied by a factor of about 1/10 to become comparable with model disks using the present normalization of ϕ_λ.

Furthermore the influence of grid shearing has been corrected by multiplying the specific intensity with an directional dependent correction factor (see Appendix A.3 for details). The correction of grid shearing has a larger influence on the line intensities than the normalization of ϕ_λ.

A.3. Ray dispersion and grid shearing

The solution of a first order differential equation on a multidimensional grid always consists of the fundamental problems of ray dispersion and grid shearing. A sharp-edged beam of light, transported on a 2D or a 3D grid in vacuum ($\kappa^\mathrm{l} = S^\mathrm{l} = 0$) is redistributed in the sense that the ray gets broader and less intense in the center. Ray dispersion consequently lowers the spatial resolution of the model grid [Kunasz & Auer 1988].

Additionally the specific intensity of the ray is only conserved for directions parallel to the diagonal $\mathbf{n}_\mathrm{D} = (1/\sqrt{3}, 1/\sqrt{3}, 1/\sqrt{3})$ of the rectangular grid. It is found that the specific intensity increases for directions $\mathbf{n} \neq \mathbf{n}_\mathrm{D}$:

$$\sigma_\mathrm{D}(\mathbf{n}) = \frac{I(\mathbf{n})}{I(\mathbf{n}_\mathrm{D})} \cong \frac{1}{\mathbf{n}_\mathrm{D}\cdot\mathbf{n}}, \tag{A1}$$

as a consequence of the shear between the rectangular grid and the direction $\mathbf{n} = (\cos\varphi\sin i, \sin\varphi\sin i, \cos i)$ of the current ray. The maximum angle between the diagonal vector $\mathbf{n}_\mathrm{D}$ and a coordinate axis is $\arccos(1/\sqrt{3}) = 54.7°$ and $\sigma_\mathrm{D}(\mathbf{n})$ can reach $\sqrt{3}$ for rays nearly parallel to the coordinate axis. The grid shearing is corrected via the anisotropic factor σ_D in Eq. 3 of Paper I by:

$$\bar{J} = \frac{1}{4\pi}\oint\int I\varphi_\lambda\frac{\mathrm{d}\Omega}{\sigma_\mathrm{D}}\mathrm{d}\lambda\ . \tag{A2}$$

References

Adam, J., 1990, A&A, 240, 541
Avrett, E.H., Hummer, D.G., 1965, MNRAS, 130, 295
Dachs, J., 1987, in A. Slettebak, T.P. Snow (eds.), Physics of Be stars, IAU Coll. 92, Cambridge Univ. Press, p. 149
Dachs, J., Hummel, W., Hanuschik, R.W., 1992, A&AS, 93, 116
Hanuschik, R.W., 1986, A&A, 166, 185
Hanuschik, R.W., 1988, A&A, 190, 187
Hanuschik, R.W., Kozok, J., Kaiser, D., 1988, A&A, 189, 147
Hanuschik, R.W., Hummel, W., Dietle, O., Sutorius, E., 1995, A&A, 300, 163
Hanuschik, R.W., Hummel, W., Sutorius, E., Dietle, O., Thimm, G., 1996, A&AS, 116, 309
Horne, K., Marsh, T., 1986, MNRAS, 218, 761
Hummel, W., 1994, A&A, 289, 458 (Paper I)
Huang, S.S., 1973, ApJ, 183, 541
Hummel, W., Dachs, J., 1992, A&A, 262, L17

Hummel, W., Vrancken, M., 1995, A&A, 302, 751
Johnson, M., 1958, in "Etoiles à raie d'emission", Institute d'Astrophysique de Liège, p.219
Kato, S., 1983, PASJ, 35, 249
Kunasz, P., Auer, L.H., 1988, JQSRT 39, 67
McLaughlin, D.B., 1961, JRASC, 55, 13 and 73
Okazaki, A.T., 1991, PASJ, 43, 75 (O91)
Papaloizou, J.C., Savonije, G.J., Henrichs, H.F., 1992, A&A, 265, L45
Poeckert, R., Marlborough, J.M., 1978, ApJ, 220, 940
Prinja, R.K., 1989, MNRAS 241, 721
Rybicky, B.G., Hummer, D.G., 1983, ApJ, 274, 380
Slettebak, A., 1982, ApJS, 50,55
Struve, O., 1931, ApJ, 73, 94
Waters, L.B.F.M., 1987, A&A, 162, 121

This article was processed by the author using Springer-Verlag LaTeX A&A style file *L-AA* version 3.